

# Segmenting and Tracking Fluorescent Cells in Dynamic 3-D Microscopy With Coupled Active Surfaces

Alexandre Dufour, Vasily Shinin, Shahragim Tajbakhsh, Nancy Guillén-Aghion, Jean-Christophe Olivo-Marin, *Senior Member, IEEE*, and Christophe Zimmer

**Abstract**—Cell migrations and deformations play essential roles in biological processes, such as parasite invasion, immune response, embryonic development, and cancer. We describe a fully automatic segmentation and tracking method designed to enable quantitative analyses of cellular shape and motion from dynamic three-dimensional microscopy data. The method uses multiple active surfaces with or without edges, coupled by a penalty for overlaps, and a volume conservation constraint that improves outlining of cell/cell boundaries. Its main advantages are robustness to low signal-to-noise ratios and the ability to handle multiple cells that may touch, divide, enter, or leave the observation volume. We give quantitative validation results based on synthetic images and show two examples of applications to real biological data.

**Index Terms**—Active contours, cell biology, cell migration, deformable models, fluorescence, level sets, segmentation, three-dimensional (3-D), tracking.

## I. INTRODUCTION

### A. Motivation

1) *Cell Motility*: The ability of many types of cells to alter their shape, divide or migrate is central to processes of major importance in biological research. Cells of the immune system, for instance, migrate toward sites of infection, where they target and bind to cells presenting antigens; upon activation, the immune cells then change their shape, allowing proteins to cluster at the interface with the antigen presenting cell [1]. In embryonic development, progenitor cells migrate along well-defined paths to reach distant sites where they will form new organs and tissues; coordinated divisions and changes of cellular morphology also play an important role in the regulation of tissue growth [2]. In tumorigenesis, cancer cells can adopt a particular “amoeboid” morphology allowing them to squeeze through the

three-dimensional (3-D) extracellular matrix and reach remote organs, leading to metastasis [3]. Similarly, many parasitic cells rely on active motion or shape changes to phagocyte, adhere to and invade host tissue [4]–[6].

Because alterations of cell shape and motion can induce or inhibit the development of pathologies, the study of cell dynamics is crucial for understanding and combatting various types of human diseases. Recent studies have shown that the motion and morphology of parasites or cancer cells in natural or artificial 3-D environments differs markedly from their behavior on two-dimensional (2-D) substrata such as glass or cell layers [3], [4], [7]. Cell dynamics will, therefore, be increasingly studied in 3-D and 3-D+time.

2) *Three-Dimensional+Time Microscopy*: Systematic observations of living cells is possible thanks to widespread availability of fluorescent markers and modern optical microscopes. For 3-D imaging, techniques of choice are confocal [8] or multiphoton microscopes, which allow optical sectioning of cells in culture or inside tissues [9], [10], leading to the acquisition of “*z* stacks” (3-D images). Importantly, however, the generated images are corrupted by considerable noise and blur. The blur stems from the diffraction limited nature of light microscopy, whereby light emitted by single fluorescent molecules is spread into an approximately ellipsoidal, cylindrically symmetric volume elongated along the optical axis (or *z* axis), and described by the point spread function (PSF). For typical imaging conditions, the confocal PSF has a full-width at half-maximum (FWHM) in the range of  $\sim 0.1$ – $0.2 \mu\text{m}$  in the two lateral directions (*x* and *y*) and  $\sim 0.5$ – $1.0 \mu\text{m}$  along the *z* axis (for comparison, crawling cells such as amoebae have sizes on the order of  $\sim 20 \mu\text{m}$ ). The blurred images are then sampled on an anisotropic grid, with voxel sizes ideally adjusted to the Nyquist criterion, though under-sampling is frequent in practice.

In addition to blur, confocal 3-D+time data also suffer from noise, whose dominant type is generally Poisson noise [11]. This is due to the small number of photons available to image each voxel, which is strongly limited by fluorophore concentrations, photo-bleaching (fluorescence decay due to chemical alterations of fluorescent molecules), and the small exposure times needed to rapidly acquire *z* stacks. As a result, 3-D+time cellular imaging data typically suffer from small signal-to-noise ratios (SNRs) (e.g., Figs. 4 and 6).

3) *Need for Quantification*: Visual inspection of such imaging data often yields important qualitative information,

Manuscript received December 1, 2004; revised June 2, 2005. This work was supported by the Institut Pasteur. The associate editor coordinating the review of this manuscript and approving it for publication was Dr. Erik Meijering.

A. Dufour was with the Quantitative Image Analysis Group, Institut Pasteur, 75724 Paris Cedex 15, France. He is now with the Institut Pasteur Korea, 136-791 Seoul, Korea (e-mail: alexandre.dufour@pasteur.or.kr).

V. Shinin and S. Tajbakhsh are with the Department of Developmental Biology, Stem Cells and Development, Pasteur Institute, 75724 Cedex 15, Paris, France (e-mail: vshinin@pasteur.fr; shaht@pasteur.fr).

N. Guillén-Aghion is with the Unité d'Biologie Cellulaire du Parasitisme, INSERM U389, Institut Pasteur, 75724 Paris Cedex 15, France (e-mail: nguillen@pasteur.fr).

J.-C. Olivo-Marin and C. Zimmer are with the Quantitative Image Analysis Unit, Institut Pasteur, 75724 Paris Cedex 15, France (e-mail: jcolivo@pasteur.fr; czimmer@pasteur.fr).

Digital Object Identifier 10.1109/TIP.2005.852790

which is sometimes sufficient to assess drastic effects on cell behavior. However, because cell motility is regulated by large networks of genes and proteins, alterations of their expression levels or concentrations rarely result in such dramatic effects. In most cases, visual inspection is insufficient to describe or even detect subtle but important changes in motility phenotypes, such as a relative increase in directionality of a correlated random walk [12], or a tendency to protrude pseudopodia in an organized fashion [13]. To adequately detect and characterize such effects, a quantitative assessment of cellular motility is required.

4) *Basic Segmentation and Tracking Methods:* Quantitative analyses of cell shape and motion primarily require segmentation and tracking of individual cells. Currently, this is mostly performed manually or using semi-automatic software tools available in microscopy software (see [9] for a representative list). Typical 3-D+time data sets consist of thousands or tens of thousands of images; thus, manual cell tracking is extremely labor-intensive, in addition to being prone to errors, user bias, and lack of reproducibility.

Tracking and segmentation tools commonly distributed with microscopy software are generally based on standard techniques such as correlation matching, thresholding, or morphological operators. Although useful for many data sets, these methods suffer restrictions that considerably limit their use for typical data sets from cell biology research. Correlation matching, for instance, fails for objects that change shape in noisy images, and generally requires the user to manually define each object's position in the first frame. Segmentation methods based on global thresholding fail for images that exhibit strong intensity gradients and/or noise. Preprocessing with smoothing filters and adaptive thresholding helps, but touching cells or nuclei will be merged. Watershed transforms can prevent merging, but usually lead to oversegmentation unless the markers are manually chosen. To overcome such limitations, commercial software tools often allow the user to interactively correct trajectories or segmentations through an adequate interface. As a result, however, the benefits of automation (speed, reproducibility, and objectivity) tend to be lost. Therefore, development of more reliable and automatic image analysis methods remains an important goal.

## B. Outline of Present Work and Related Efforts

Here, we present a fully automatic method for segmentation and tracking of multiple cells from time series of 3-D microscopy data. The method is specifically designed to process data with low SNRs due to photon-limited imaging, and allow tracking of cells that tend to touch each other.

1) *Active Contour Methods:* Basic image processing techniques such as those mentioned above, which operate according to local pixel properties only, are ill suited to handle these difficulties. In line with many others, we believe that they are best addressed using a model-based segmentation approach, which allows the incorporation of *a priori* knowledge about global object properties. To do this, we adopted the framework of active contours and surfaces, which is employed widely and successfully in computer vision and medical imaging [14]–[17] and has

been used by different groups to track cells in 2-D time lapse microscopy [18]–[23] and to segment cells from static 2-D images [24]. In these methods, objects are represented as closed contours or surfaces (fronts), that evolve with a speed computed from both image-dependent data and image-independent geometric properties. The evolution equation for the front is often derived from the minimization of an energy functional containing a data attachment constraint—defined such as to be minimum when the front follows object boundaries—and *a priori* constraints, which act as regularizers for ill-posed problems. Once a segmentation is achieved for the current (2-D or 3-D) image, the resulting front can be used to initialize segmentation of the next image, provided that motions between consecutive imaging times are modest, thereby achieving tracking [14], [18], [25].

We now discuss relevant work on active contours and briefly outline the main technical choices of the method presented in this paper.

2) *Region versus Boundary Oriented Methods:* Active contour methods require specifying a data attachment term, for which many different choices have been proposed. Earlier methods used boundary oriented data attachment terms, which depend only on the integral of a locally computed edge map, such as the magnitude of the intensity gradient, along the contours [14], [26], [27]. Strong gradients at object boundaries may indeed be expected for cells stained with fluorescent membrane markers, or highly concentrated nonspecific (cytoplasmic) markers. However, these gradients are washed out by blur and equally strong gradients may arise elsewhere due to noise (see Section I-A.2) or to in-homogeneous staining caused by intracellular structures (see, e.g., Fig. 4). Purely edge based active contours usually fail on such cell images, unless a very good initialization is provided. In contrast, region-oriented active contours, or “active regions,” which position the boundary according to statistical information computed over the whole image domain [28]–[31], are much more tolerant to noise, spurious structures, and inaccurate initialization. Gradient information can nevertheless be used in combination to region information, as done, e.g., by [32], to refine the localization of boundaries that may exhibit significant intensity gradients. The image model of our method employs both a gradient term and a region model, adopted from Chan and Vese [31], which is able to segment objects with ill-defined edges.

3) *Explicit versus Implicit Active Contours:* Another essential choice in active contour methods is the mathematical representation of the front. In explicit methods, the fronts are represented parametrically, and the evolution of control points is computed in a Lagrangian fashion [14], [18], [33]. In implicit methods, the fronts are defined as the zero level set of a scalar function defined over the image domain [26], [30], [31], [34], whose evolution is computed using Eulerian equations. Implicit methods naturally allow the evolving front to split and merge, which allows the segmentation of an arbitrary number of disjoint objects from an arbitrary initial front. This in turn enables automatic initialization, automatic detection of incoming cells, and automatic handling of cell divisions. Similar topological flexibility can be introduced into parametric active contours, but this requires complicated “surgical” schemes [33], [35]. Extension

of the parametric approach to 3-D is a nontrivial task, whereas implicit methods are well suited to capturing 3-D surfaces as complex as the cortex of the brain [36]–[38]. For these reasons, we adopted the implicit representation in this work.

4) *Multiple Level Set Methods*: Besides their well known computational complexity, an important limitation of implicit methods is that the generally advantageous topological flexibility can become undesirable in cases where the topology of objects is known or constrained independently of the data [21], [38], [39]. This is the case in cell tracking, when cells previously identified as distinct objects move together and touch, causing their associated fronts to merge. This merging violates the *a priori* knowledge that the cells themselves remain separate entities, and leads to a breakdown of both segmentation and tracking [21], [39]. To overcome this difficulty, we use multiple level set functions, one for each cell, and introduce an overlap penalty to inhibit merging of neighboring active surfaces. This is an extension to 3-D of the model we proposed in [39], itself closely related to other multiple active contour methods [23], [29], [30], [40]–[43]. Two coupled active surfaces have also been used before for static 3-D brain image segmentation by [36], [37]. In contrast to [29], [36], [37], and [41], the number of level set functions in our method is not related to classes of image intensity, but is determined by the number of objects to be tracked. This allows preservation of the identity of cells even if they touch and their intensities are similar.

The rest of the paper is organized as follows. Section II describes our cell segmentation and tracking method, Section III gives validation results on simulated data, Section IV shows illustrations on real data, and Section V concludes the paper.

## II. METHOD

This section describes in more detail the technical choices of our segmentation and tracking method.

### A. Active Surfaces With and Without Edges

Our method is based on the active contours without edges introduced (for 2-D images) by Chan and Vese [31]. This model seeks to partition the image by minimizing the piece-wise constant Mumford–Shah functional for image segmentation. The functional contains two data attachment terms that penalize the variance of the intensity inside and outside the boundary, and a regularization term that penalizes the total boundary length. It is, thus, suited to cells stained with fluorescent dyes that diffuse throughout the cell cytoplasm, which appear as regions of average intensity larger than that of the background. Despite the binary character of the model, it is tolerant to substantial inhomogeneities of the intensity, such as those caused by intracellular structures, as will be seen in Section III. To account for the possible presence of edge information, we replace the length penalty of [31] by a more general geodesic length, whose metric is computed from an image edge map [27]. As mentioned in Section I-B.2, this addition is useful to refine the segmentations of boundaries, particularly for cells with fluorescently labeled membranes.

Although the model [31] was described for 2-D images, its extension to 3-D is straightforward thanks to the level set

representation. Our functional for 3-D active surfaces with or without edges, thus, reads

$$E(S, c_I, c_O) = \iint_S \alpha g dS + \lambda_I \iiint_{\text{inside}(S)} (I - c_I)^2 dx dy dz + \lambda_O \iiint_{\text{outside}(S)} (I - c_O)^2 dx dy dz. \quad (1)$$

In this expression,  $S$  is the set of surfaces that defines the image partition,  $dS$  is the elementary surface area,  $c_I$  and  $c_O$  are previously unknown scalar variables, and  $I = I(x, y, z)$  is the image intensity at the location  $(x, y, z) \in \Omega$ ,  $\Omega \subset \mathbb{R}^3$  being the image domain. The function  $g$  is defined as  $g = 1/(1 + \lambda_e f)$ , where  $f$  is an edge map of the image, chosen depending on the type of fluorescent labeling. For cytoplasmic dyes, one can take the gradient magnitude of the image smoothed by a Gaussian kernel:  $f = |\nabla(G_\sigma * I)|$ . For dyes that preferentially stain the cell membrane, a better choice is  $f = G_\sigma * I$ . Finally,  $\alpha$ ,  $\lambda_e$ ,  $\lambda_I$ , and  $\lambda_O$  are fixed positive parameters, which must be adjusted empirically. Note that one can set  $\lambda_I = 1$ , without loss of generality, since the minimization problem is unchanged if  $E$  is replaced by  $E/\lambda_I$ . Also note that with  $\lambda_e = 0$ , the geodesic length term [27] reduces to the Euclidian length as in [31].

Following the level set representation [34], the set of surfaces  $S$  is defined implicitly as  $\phi^{-1}(0) = \{(x, y, z) \in \Omega | \phi(x, y, z) = 0\}$ , where  $\phi$  is a scalar function (the level set function) defined over  $\Omega$ . The functional (1) can then be expressed directly as a function of  $\phi$  [31]

$$E(\phi, c_I, c_O) = \iiint_{\Omega} [\alpha g \delta(\phi) |\nabla \phi| + \lambda_I H(\phi) (I - c_I)^2 + \lambda_O (1 - H(\phi)) (I - c_O)^2] dx dy dz \quad (2)$$

where  $H$  and  $\delta$  are the Heaviside and Dirac functions, respectively, and we use the convention that  $\phi > 0$  inside closed surfaces and  $\phi < 0$  outside.

Starting from an initialization  $\phi_{t=0}(x, y, z)$ , the minimization of (2) is accomplished by letting the level set function evolve as function of an abstract time  $t$  according to

$$\frac{\partial \phi}{\partial t} = \left[ \alpha g \nabla \cdot \frac{\nabla \phi}{|\nabla \phi|} + \alpha \nabla g \cdot \frac{\nabla \phi}{|\nabla \phi|} - \lambda_I (I - c_I)^2 + \lambda_O (I - c_O)^2 \right] \delta(\phi) \quad (3)$$

while the variables  $c_I$  and  $c_O$  are the mean intensity of voxels inside and outside the current zero level set, respectively

$$c_I(t) = \langle H(\phi) \rangle; \quad c_O(t) = \langle 1 - H(\phi) \rangle \quad (4)$$

where

$$\langle f \rangle = \frac{\iiint_{\Omega} I f dx dy dz}{\iiint_{\Omega} f dx dy dz} \quad (5)$$

is the average of the intensity weighted by  $f$  over  $\Omega$ . The implementation of (3) and (4) uses smooth infinite support approximations of  $H$  and  $\delta$ . For further details we refer to [31].

This model of active surfaces with or without edges has two important benefits that make it particularly useful for fluorescent microscopy images. First, it does not require sharp boundaries and is able to segment fuzzy objects including blurred and noisy cells. Nevertheless, if the staining produces strong gradients or intensities at the cell membrane, the method can use them to improve segmentations. Second, contrary to other region based active contours [28], [29] the model does not require prior knowledge of the intensity characteristics of the object. In particular,  $c_I$ , which upon successful segmentation is the average intensity of the segmented object, is computed self-consistently by the algorithm. The model only requires an average intensity contrast between the background and the cell.

### B. Coupling Multiple Active Surfaces

Besides noise and blur, a major difficulty of cellular imaging is that cells are rarely observed isolated, but generally appear in groups and often touch each other. With the implicit representation, a single level set function can be used to represent an arbitrary number of objects, in contrast to explicit methods, which require initialization by a distinct contour for each object [20], [21]. The binary model using one level set  $\phi$  described in Section II-A is indeed able to segment a collection of spatially isolated cells. It is suboptimal, however, if cells have significantly different average intensities (which they do when absorbing different concentrations of fluorescent molecules as in Fig. 4), because the average intensity  $c_I$  is taken over all cells and does not account for intensity differences between them. A more severe limitation occurs when two or more cells come in contact, since the single level set model will incorrectly identify them as a single object [39].

Both of these limitations can be overcome by using multiple level set functions. In [41], Vese and Chan described a multiphase extension of their model [31] where  $\log_2 n$  level set functions are used to efficiently represent  $n$  classes. However, these classes lump together objects of similar intensities; thus, the multiphase model fails to distinguish touching cells unless their average intensities are significantly different. In addition, some of the  $n$  classes may be empty; thus, the effective number of objects can vary depending on parameter settings. This contradicts the *a priori* knowledge that the number of imaged cells remains constant, except if cells divide, enter or leave the observation volume (these three events can be identified based on the location and shape of detected cells). Therefore, we instead choose to represent each cell  $i$  ( $i = 1 \dots n$ ) by its own level set function  $\phi_i$ , and use an overlap penalty to discourage active surfaces from crossing each other. We, thus, now consider the following functional, defined on all level set functions simultaneously:

$$\begin{aligned} E(\phi_1, \dots, \phi_n, c_O, c_{I,1}, \dots, c_{I,n}) \\ = \iiint_{\Omega} \sum_{i=1}^n \left[ \alpha g \delta(\phi_i) |\nabla \phi_i| + \lambda_I H(\phi_i) (I - c_{I,i})^2 \right. \\ \left. + \frac{\lambda_O}{n} \prod_j (1 - H(\phi_j)) (I - c_O)^2 \right. \\ \left. + \gamma \sum_{i < j} H(\phi_i) H(\phi_j) \right] dx dy dz. \end{aligned} \quad (6)$$

The terms weighted by  $\alpha$ ,  $\lambda_I$  and  $\lambda_O$  are almost identical to those in the single level set functional (2), except for the factor  $\prod_j (1 - H(\phi_j))$ , which is the indicator function of the region outside all  $n$  active surfaces and accounts for the fact that there is only one background. The term weighted by  $\gamma$  is equal to the summed volumes of pair-wise intersecting active surfaces [since  $H(\phi_i)H(\phi_j)$  is the set indicator function of the region inside both  $S_i$  and  $S_j$ ]. The minimization of this term, thus, tends to remove overlaps between distinct surfaces. Two-dimensional equivalents of this model, both with implicit and parametric contours, were described by us in [39] and [23], respectively.

The following  $n$  evolution equations can be derived from the Euler–Lagrange equations associated to the minimization of (7):

$$\begin{aligned} \frac{\partial \phi_i}{\partial t} = \left[ \alpha g \nabla \cdot \frac{\nabla \phi_i}{|\nabla \phi_i|} + \alpha \nabla g \cdot \frac{\nabla \phi_i}{|\nabla \phi_i|} - \lambda_I (I - c_{I,i})^2 \right. \\ \left. + \lambda_O \prod_{j \neq i} H(\phi_j) (I - c_O)^2 - \gamma \sum_{j \neq i} H(\phi_j) \right] \delta(\phi_i) \end{aligned} \quad (7)$$

where

$$c_{I,i}(t) = \langle H(\phi_i) \rangle; \quad c_O(t) = \left\langle \prod_j (1 - H(\phi_j)) \right\rangle. \quad (8)$$

As a result of the level set representation, these equations are identical to their 2-D counterpart in [39] [except for the triple integrals in (5)]. The effect of the  $\gamma$  term in (7) is clear: at voxels located inside surfaces other than  $S_i$  (where  $\sum_{j \neq i} H(\phi_j) > 0$ ), this term is negative, causing  $\phi_i$  to decrease, and  $S_i$  to recede from this location. The recession speed is higher in regions where more than two active surfaces overlap.

### C. Volume Conservation Constraint

The repulsive coupling introduced above prevents neighboring active surfaces from overlapping and, thus, maintains the identity of touching cells. However, since it does not involve image data, this constraint does not favor any particular location for the boundary between touching objects. When cells of similar fluorescence levels touch, the image content is often insufficient to outline the boundary between cells, even for a human expert. In such cases, segmentation results will generally be incorrect, because the image dependent terms in (7) are unable to guide the surface toward the correct location; active surface evolution then depends primarily on initialization and the curvature term [first term inside brackets of (7)], which causes active surfaces to shrink and vanish. Additional *a priori* information on the objects, if available, can help improve segmentation results in cases where the data attachment term is insufficient. An example of such a constraint is the requirement that cells be approximately round used to track leukocytes in [20]. Since our goal here is to track cells that generally move by actively changing their shape, we cannot use such a strong constraint.

Instead, we use the much weaker constraint that cell volumes remain approximately constant during the time of observation. This is justified by the fact that most cells including motile cells are known to regulate osmotic fluxes to maintain constant volumes, a process known as volume homeostasis [44].

If  $V_{i,0} = \iiint_{\Omega} H(\phi_{i,0}) dx dy dz$  is the volume of cell  $i$  as computed from segmentation of the first  $z$  stack, the volume conservation constraint is easily expressed as

$$E_{V,i}(\phi_i) = \eta_i \left( \iiint_{\Omega} H(\phi_i) dx dy dz - V_{i,0} \right)^2 \quad (9)$$

where  $\eta_i$  is the weight of the constraint, which may depend on the considered cell (see below). The penalty (9) is then added inside the bracket of (6). In the evolution equation (7), this leads to an additional term  $-2\eta_i(\iiint_{\Omega} H(\phi_i) dx dy dz - V_{i,0})$  inside the bracket.

The volume conservation constraint was observed to considerably improve the segmentation of touching cells, by avoiding, for instance, that one active surface engulfs two touching cells while the other surface collapses. In addition, this constraint helps to counteract the detrimental effect of bleaching, which might otherwise cause an apparent contraction of the segmented cell volumes over time due to a decrease of the cell intensity relative to that of the background. Volume conservation is violated, however, for cells that undergo divisions or cross the boundaries of the observation volumes. For these cells, the parameter  $\eta_i$  can simply be set to zero.

#### D. Tracking Scheme

In this section, we describe how the active surfaces are used for tracking cells in 3-D+time image sequences.

We temporarily assume that cells are spatially isolated on the first  $z$  stack of the sequence. At the moderate cell densities for which our method is designed, this is the most frequent case (the case of initially touching cells will be discussed below). A single level set  $\phi$  is used to detect these isolated cells and allowed to evolve according to (3) and (4) until convergence. Once the first  $z$  stack has been segmented, we identify the  $n$  connected components  $O_i$  of the segmentation. For all  $i, i = 1 \dots n$ , we compute a new level set function  $\phi_i$  from the signed distance function to the boundaries of  $O_i$ , with positive values inside  $O_i$  and negative values outside  $O_i$ . These  $n$  level set functions are then used to initialize the evolution of coupled surfaces according to (7) and (8). This produces an improved segmentation of the first image, because each  $c_{I,i}$  can adapt to the possibly different average fluorescence level of each cell. The  $n$  level set functions are then propagated to the second  $z$  stack to initialize segmentation by coupled surface evolutions, and similarly to all remaining  $z$  stacks, sequentially. This scheme requires that the two spatial regions occupied by a cell in two consecutive  $z$  stacks overlap, i.e., that cells do not move by more than their diameter during the time interval between acquisition of two  $z$  stacks. For displacements larger than the cell diameter, this tracking method fails.

An additional level set function  $\phi_0$  can be used to detect cells located close to the boundaries of the observation volume entering it at a later time. Connected components detected in that way will lead to the creation of new  $\phi_j$  from signed distance functions as after segmentation of the first  $z$  stack. The only other situation that can trigger creation of a new level set function is a cell division event, which can be identified after segmentation as the separation of an already existing active surface into two connected components.

A difficulty for our method is posed by cells that touch at the beginning of the sequence. In general, initially touching cells must be separated manually, because there is no obvious way to automatically distinguish them from a single, bigger cell. If two initially touching cells later move away from each other, this will be interpreted incorrectly as a cell division. In the special case where cell divisions can be ruled out, a solution is to consider the segmentation obtained after all detected (false) division events, and use it as initialization to process the sequence backward.

In summary, our approach enforces the known constraint that cells can neither disappear nor appear unless they cross the observation volume or divide.

A useful option, also discussed in [23], is to hold the coefficients  $c_{I,i}$  and  $c_O$  constant during the evolution of the  $\phi_i$  using final values from the segmentation of the previous  $z$  stack. This is justified as long as the mean cell fluorescence does not change strongly from one  $z$  stack to the next. In this manner, the unknowns  $c_{I,i}$  are set approximately to their target values from the onset of segmentation. This is advantageous for two reasons. First, computation time is saved, since the volume integrals in (4) and (5) do not need to be reevaluated at each iteration. Second, and more importantly, the evolution of active surfaces is then significantly less sensitive to initialization. As a result, good segmentations can be obtained even if the overlap between the initial surface and the object is small, as long as it is not empty. With this option, the tracking method can, thus, handle displacements as large as the size of the object. Finally, to take into account progressive changes in cell intensity, as the fluorescence decay due to bleaching, the average intensities (4) can be updated once for each  $z$  stack after segmentation.

#### E. Optimizations

A notorious disadvantage of implicit methods is their considerable computational complexity compared to explicit methods [33], [35], since the level set function has the same dimension as the image, i.e., one dimension more than the object boundary. This drawback is particularly limiting when analyzing 3-D+time data sets, which can typically reach several Gigabytes. Although processing can be done offline, reducing computation time is still highly desirable. We address this by a combination of several schemes. First, we employed the widely used narrow band technique, in which the level set function is updated only within a narrow band around the current zero level set surface [45]–[47]. Second, we seek to initialize the active surfaces as close as possible to the actual cell boundaries, in order to limit the number of iterations required for convergence. For tracking already identified cells, this is achieved by initializing with the segmented surface from the previous time point as already described. For the first  $z$  stack, in contrast, no prior knowledge is available about the cell positions.

To compute an initialization surface for the first  $z$  stack, we have, therefore, adopted the fast optimization scheme recently proposed in [48], an alternative, non-PDE based technique to minimize (1) that considers each voxel  $(i, j, k)$  separately and changes the sign of  $\phi(i, j, k)$  (i.e., switches the voxel class from inside to outside or vice-versa) whenever this decreases a discretized version of (1). Starting from an initial partition  $H_0$ , this method generally achieves a crude initial segmentation of the

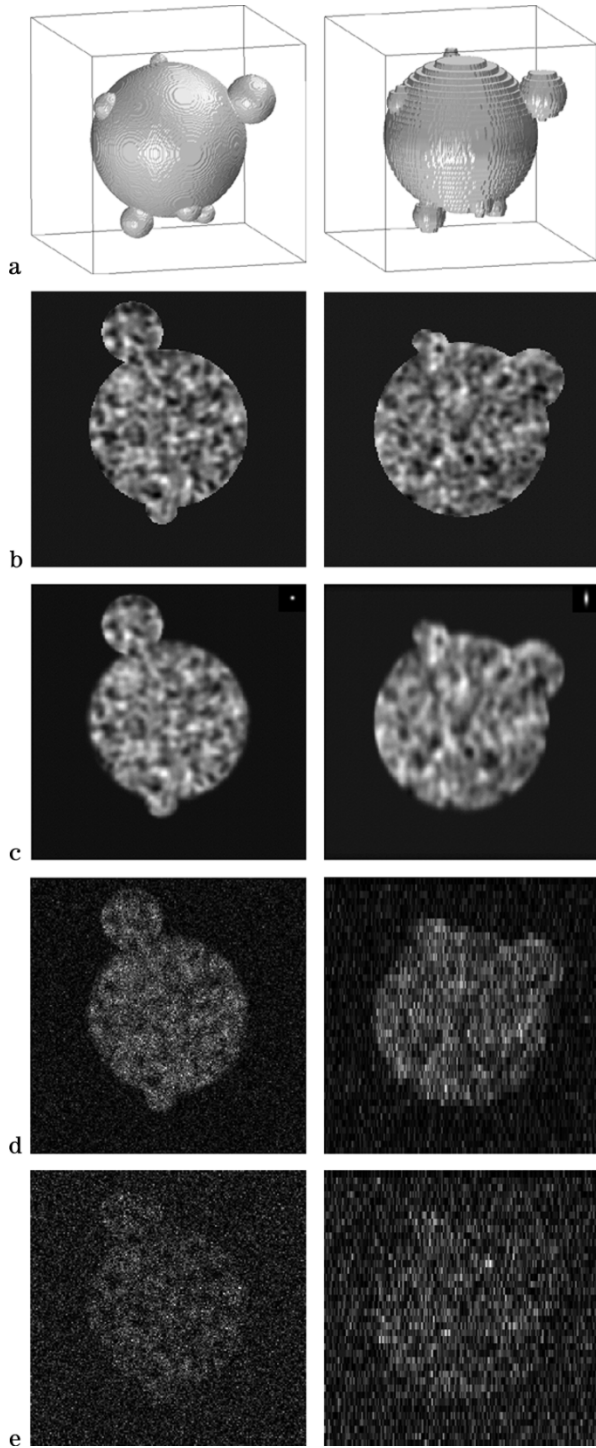


Fig. 1. Generation of a synthetic 3-D image of a deformable cell. (a) Surface rendering of a synthetic cell shape, sampled on (left) the isotropic  $200 \times 200 \times 200$  grid and (right) the anisotropic  $200 \times 200 \times 40$  grid. The  $z$  axis is vertical. Rows (b)–(e) show two cuts of the 3-D image at different steps of the data generation procedure. Left panels show a horizontal ( $xy$ ) cut; right panels show a  $yz$  cut, with vertical  $z$  axis. (b) Image of a synthetic cell object with a nonuniform interior on a uniform nonzero background, on the isotropic grid. (c) Same as (b), but blurred with an anisotropic gaussian kernel, shown as inset in the upper right corner. (d)–(e) Same as (c), but corrupted with Poisson noise and sampled on the anisotropic grid; SNR values (as defined in the text) are 2.5 in (d) and 0.5 in (e).

image within a few iterations only, but is not guaranteed to converge to a local minimum on grey-level images [48]. We ob-

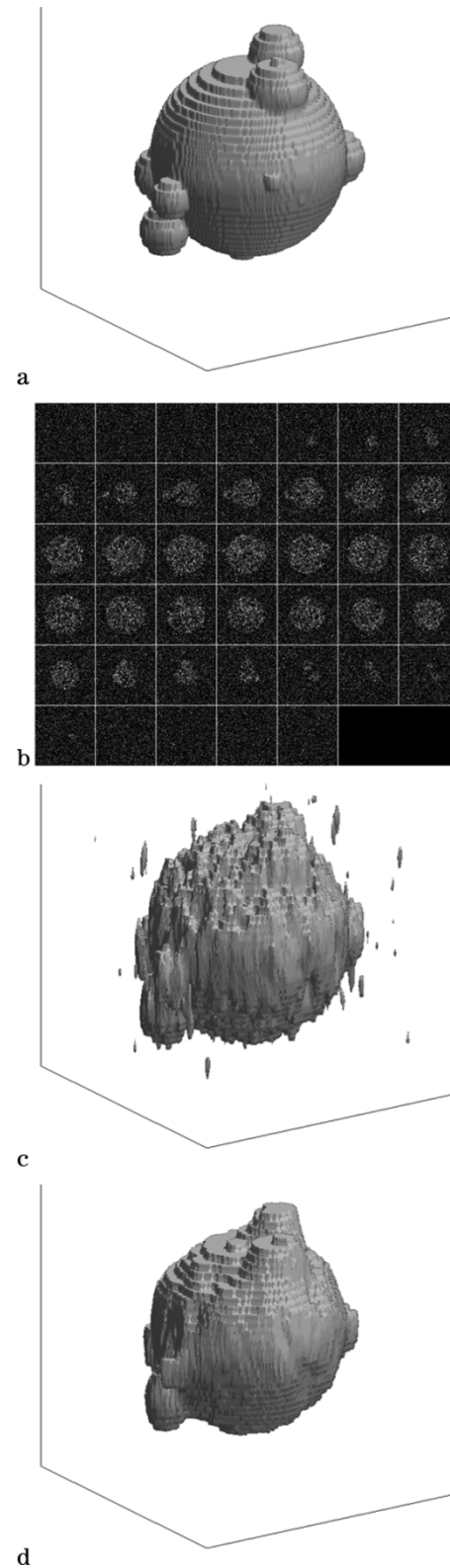


Fig. 2. Segmentation of a test image. (a) A 3-D visualization of the binary image of a synthetic object, used as ground-truth in the validation. (b) Montage of the 40 slices of the 3-D image created as described in Section III-A, with  $\text{SNR} = 0.5$ . (c) Segmentation by nonlinear diffusion filtering followed by automated thresholding. (d) Segmentation with the proposed active surface method.

served that this presegmentation is independent of  $H_0$  if the fast optimization scheme is used with  $\alpha = 0$ . Therefore, our

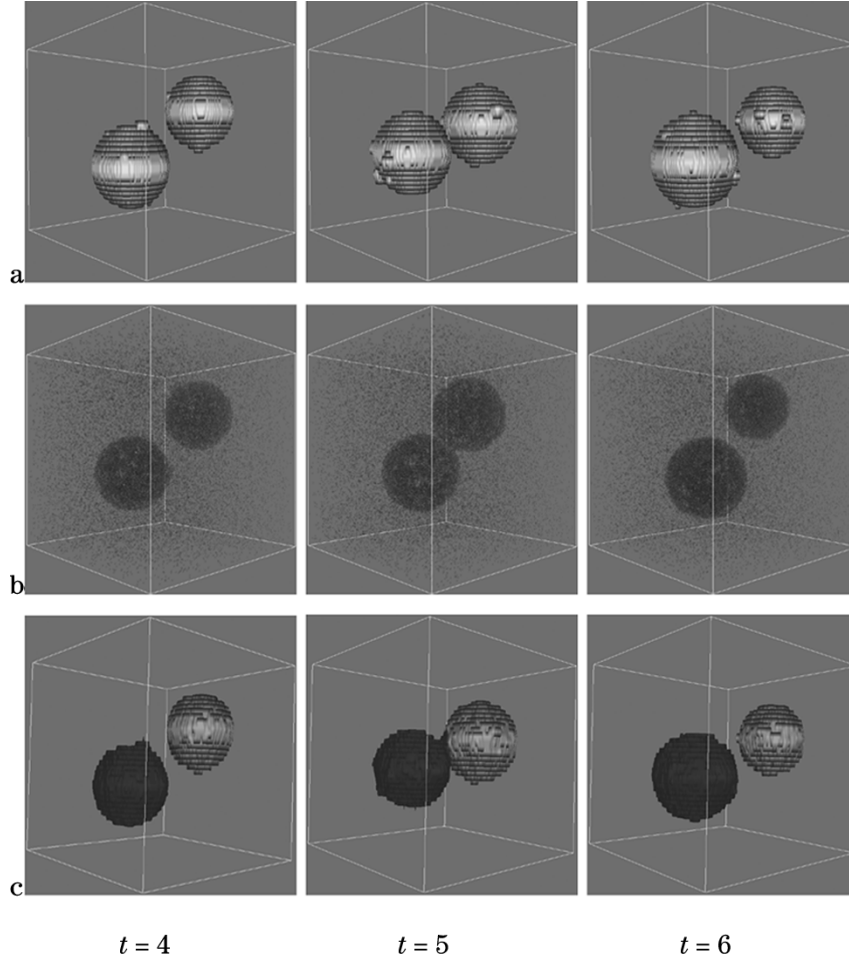


Fig. 3. Synthetic 3-D sequence of a cell contact event. (a) Synthetic binary images. (b) Synthetic noisy images. (c) Segmentation result.

TABLE I

EVALUATION OF SEGMENTATION QUALITY FOR SYNTHETIC  $z$  STACKS. FOR EACH SNR, SEGMENTATIONS WERE PERFORMED ON 100  $z$  STACKS OF SIZE  $200 \times 200 \times 40$ . TABULATED VALUES ARE THE PERCENTAGES OF MISCLASSIFIED VOXELS RELATIVE TO THE TOTAL NUMBER OF OBJECT VOXELS, AVERAGED OVER ALL  $z$  STACKS. VALUES INSIDE BRACKETS ARE THE RESULTS OBTAINED WITH THE MODEL-FREE METHOD (NONLINEAR DIFFUSION [49]) AND AUTOMATED THRESHOLDING [50]). FOR THE TWO RIGHTMOST COLUMNS, MISCLASSIFIED VOXELS WERE IGNORED IF LOCATED AT A DISTANCE LESS THAN 1 OR 2 VOXELS FROM THE TRUE OBJECT SURFACE. NOTE THAT ERRORS ARE CONCENTRATED IN THE VICINITY OF THIS SURFACE

SNR	All errors	Errors at distance	Errors at distance
		$> 1$	$> 2$
2.5	3.75% (5.12%)	0.12% (0.13%)	0.02% (0.02%)
1.5	5.36% (7.46%)	0.22% (0.29%)	0.09% (0.09%)
0.5	11.63% (16.97%)	2.24% (6.6%)	0.61% (4.12%)

segmentation procedure for the first  $z$  stack consists of the following steps: i) non-PDE based minimization of (1) with  $\alpha = 0$  (a few iterations only), ii) non-PDE based minimization of (1) with  $\alpha \neq 0$  (a few iterations only), iii) PDE-based minimization of (1) with  $\alpha \neq 0$  as described in II-A, iv) detection of connected components  $O_i$  and computation of signed distance functions, as described in II-D, and v) PDE-based minimization of (7), as described in II-B.

TABLE II

EVALUATION OF SEGMENTATION/TRACKING PERFORMANCE ON SYNTHETIC 3-D+TIME DATA INCLUDING A CONTACT EVENT. THIRTY TEST SEQUENCES WERE CONSTRUCTED AS DESCRIBED IN III-A FOR SNR = 2.5. FIRST COLUMN: AVERAGE BACKGROUND/CELLS CONFUSION, AS DEFINED IN THE TEXT AND IGNORING MISCLASSIFIED VOXELS AT DISTANCES  $< 2$  FROM THE TRUE SURFACES. OTHER COLUMNS: AVERAGE CELL/CELL CONFUSION, AS DEFINED IN THE TEXT, BEFORE, DURING, RIGHT AFTER THE CONTACT EVENT, AND AT THE END OF THE SEQUENCE

Background/cells confusion at distance $> 2$	Cell/cell confusion			
	before contact	during contact	right after contact	at the end of sequence
0.06%	0%	0.65%	0.13%	0 %

As a result of these optimizations, typical processing times for a  $z$  stack of size  $200 \times 200 \times 40$  are on the order of 1 min on a PC with a 2.2-GHz AMD Opteron 64 processor.

### III. VALIDATION ON SYNTHETIC DATA

Quantitative validation of our technique on real 3-D+time data is difficult, because it is very hard to obtain a ground-truth, since manual segmentation of possibly touching cells from low SNR microscopy  $z$  stacks is a particularly laborious and ambiguous task, even for experts. We will show examples of appli-

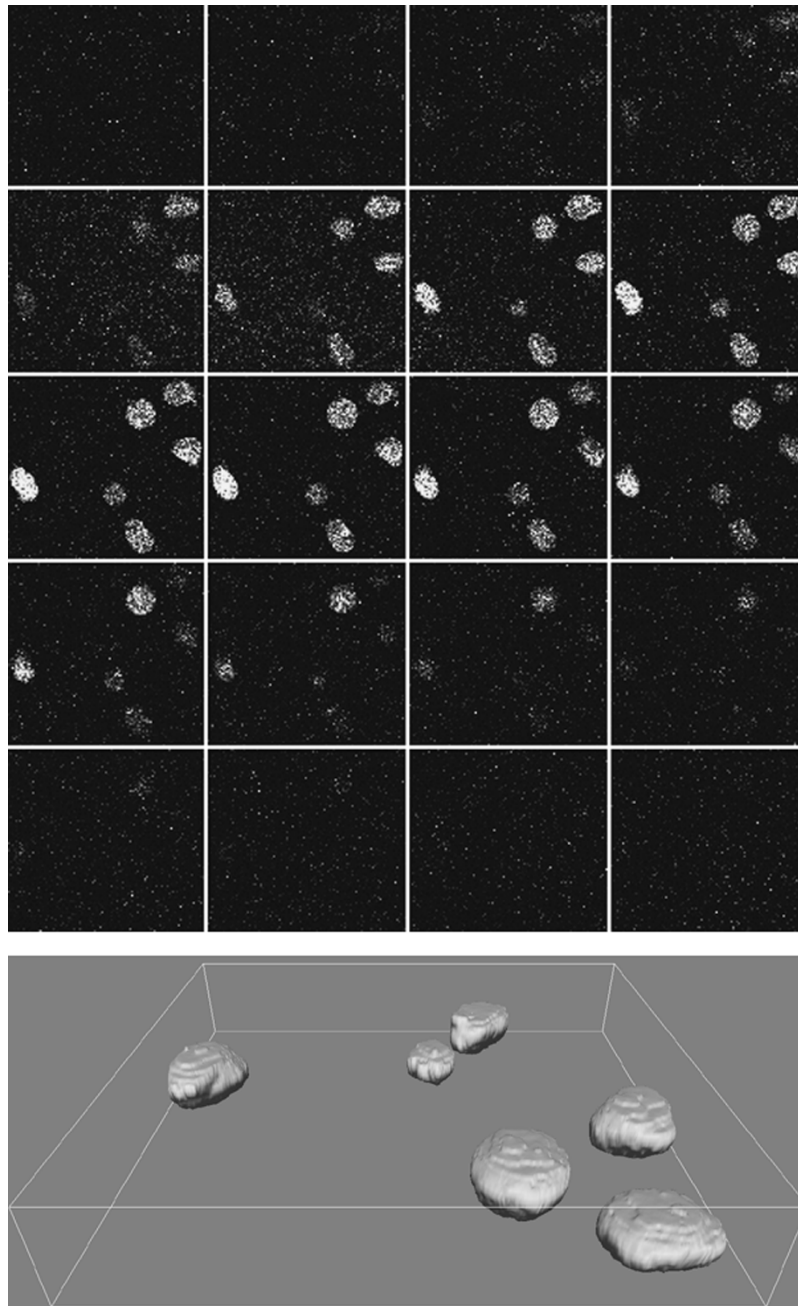


Fig. 4. Segmentation of amoebae imaged inside a 3-D tissue. Top: Montage of the image slices making up the  $z$  stack. Bottom: 3-D rendering of the segmentation result. Image size is  $432 \times 400 \times 20$ .

cations to real data in Section IV. For quantitative evaluation of our method's performance, however, we now turn to synthetic data.

#### A. Generation of Synthetic 3-D Images

Our method is designed to segment and track deformable cells such as amoebae in noisy images from confocal microscopy. To generate the synthetic data, we choose to create images that exhibit the main difficulties of real images for automated processing, rather than creating images best resembling the real data. Our data generation scheme consists of the following steps.

Step 1: We construct geometric objects representing deformable cells consisting of a central sphere of radius  $R_0$ ,

chosen randomly between 30 and 45, from which a set of five to ten small spheres are budding out with random radii between  $0.1R_0$  and  $0.2R_0$  [see Fig. 1(a), left]. The centers of the smaller spheres are placed at random locations within a range of distances from the main sphere center that allows the creation of concavities on the outer object surface. We believe that the objects generated in this way display sufficient shape variability to predict the performance of our algorithm on “roundish” deformable cells, such as amoebae with pseudopodia, or cell nuclei of most cell types. We generate a 3-D binary mask of the object on a high resolution isotropic  $200 \times 200 \times 200$  voxels grid [see Fig. 1(a), left].

Step 2: We create a nonuniform, spatially correlated distribution of intensity inside the object. This mimics the fact that



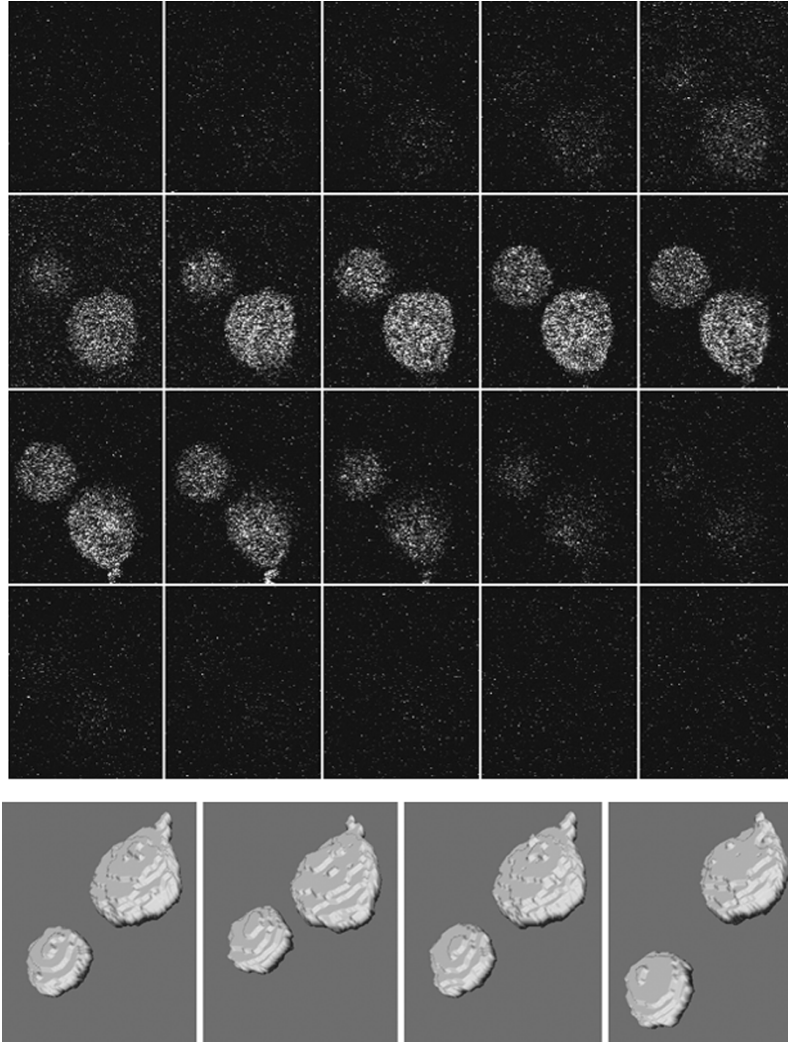


Fig. 5. Tracking two amoebae undergoing a quasicontract event. Top: Montage of a  $z$  stack from the sequence. Bottom: 3-D rendering of the segmentation result. The size of each 3-D image is  $126 \times 156 \times 20$ .

fluorescent molecules diffusing freely throughout the cell cytoplasm can nevertheless concentrate preferentially inside specific intracellular structures, such as vesicles. To do this, we first create a 3-D image of constant intensity on the isotropic grid, corrupt it with additive gaussian noise, and then blur it with a 3-D gaussian convolution kernel of standard deviation  $\sigma = 3$ . Finally, we apply the binary mask obtained in Step 1 to carve out the object and set background voxels to a given constant intensity, chosen to be lower than the mean object intensity [see Fig. 1(b)]. The mean object and background intensities determine the SNR of the final images (see below).

Step 3: To mimic the anisotropic blur caused by diffraction, we now convolute the images obtained in Step 2 with a 3-D gaussian kernel of standard deviation  $\sigma_{xy} \approx 1$  in the two horizontal directions and  $\sigma_z \approx 3$  in the axial direction. The dimensions (FWHM) of this kernel along the three axes are consistent with those of a confocal PSF for typical imaging conditions of living cells. The resulting images [Fig. 1(c)] show blurred object edges, with more pronounced blur along the  $z$  axis [Fig. 1(c), right].

Step 4: We down-sample the images obtained in Step 3 on an anisotropic  $200 \times 200 \times 40$  voxel grid, with voxels elongated along the  $z$  axis by a factor 5. This accounts for the fact

that 3-D microscopy images are often under-sampled along the  $z$  axis, as mentioned in Section I-A.2 (we also down-sample the binary object mask of Step 1 on this grid [see Fig. 1(a) right and Fig. 2(a)]; this 3-D image will serve as a ground-truth for validation in Section III-C). Finally, we simulate Poisson noise due to photon counting. By changing the average intensity of the background ( $I_b$ ) and the object ( $I_o$ ) used in Step 2, we let the SNR—defined here as the ratio between the mean object intensity above the background intensity and the standard deviation of noise—take on values 2.5 ( $I_b = 2$ ,  $I_o = 6$ ), 1.5 ( $I_b = 1$ ,  $I_o = 3$ ) and 0.5 ( $I_b = 2$ ,  $I_o = 3$ ) [see Figs. 1(d) and (e) and 2(b)]. At the lowest SNR, the objects are hardly visible to the naked eye [Figs. 1(d) and 2(b)].

In summary, our synthetic 3-D images of cell-like objects were constructed to exhibit the main characteristics of the targeted real images: roundish shapes with random deformations possibly including concavities, object intensity in-homogeneities, anisotropic diffraction blur, Poisson noise, and anisotropic sampling.

#### B. Generation of 3-D+Time Data

To test the ability of our method to track moving and deforming cell objects in time, we generated 3-D+time data of two

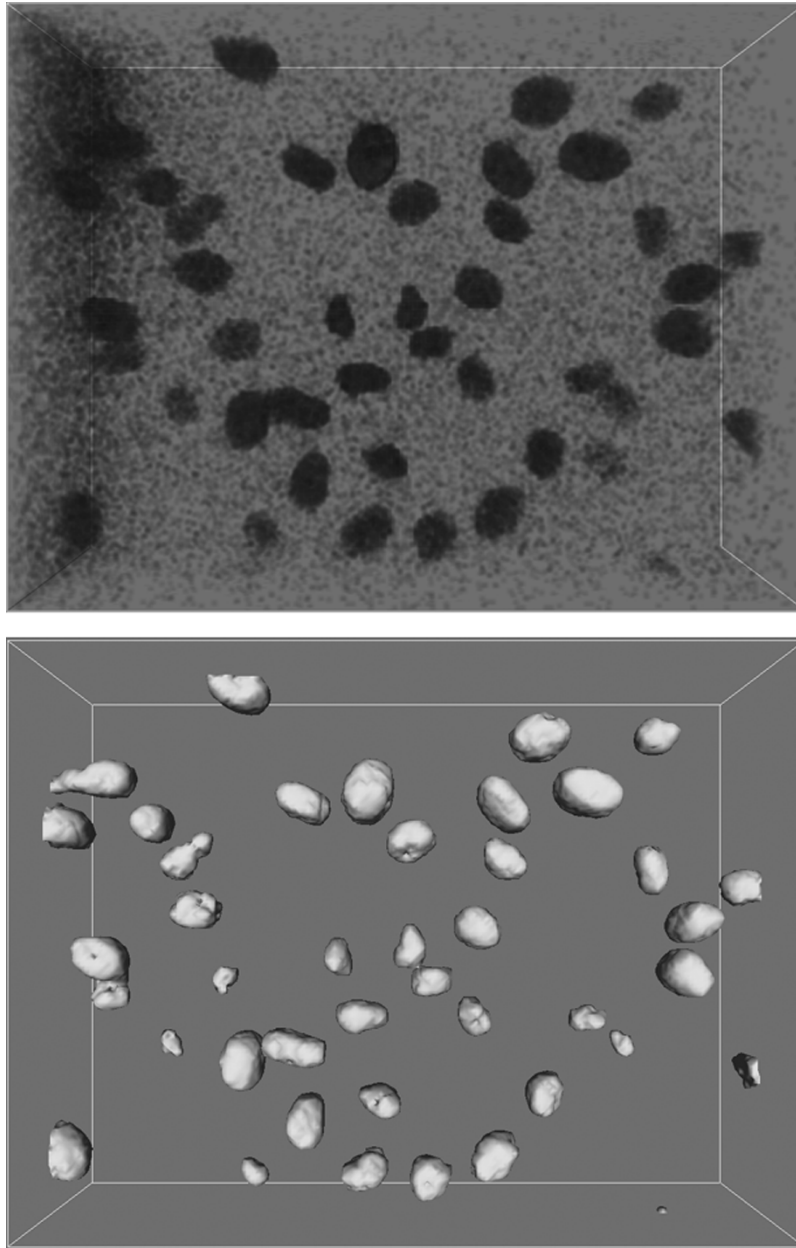


Fig. 6. Segmenting stained nuclei of proliferating MDCK cells. Top: 3-D visualization of the image stack. Bottom: Segmentation result. Image size:  $672 \times 512 \times 45$ .

objects undergoing contacts. To do this, we first two created trajectories, then generated a 3-D image for each time point as described in Section III-A, using the current positions as the centers of the two main spheres. The trajectories were built using 3-D displacements with random orientation and length  $d < R_0$ , under the constraint that the objects do not leave the image volume. To create contact events, we additionally required that the two objects i) be spatially isolated at the beginning and the end of the sequence and ii) touch at least once during the sequence.

### C. Segmentation Performance on 3-D Images

We first evaluate the performance of our method with regards to segmenting spatially isolated objects. We also compare our

results with segmentations obtained using Perona and Malik's nonlinear diffusion filtering [49] followed by Otsu's [50] automatic thresholding. The latter method was chosen as a representative example of a model-free segmentation approach. For this evaluation, we processed 300  $z$  stacks generated as described in Section III-A. Fig. 2(b) shows such a  $z$  stack together with the ground-truth [Fig. 2(a)] and segmentation results [Fig. 2(c) and (d)].

A crucial requirement for any segmentation method is that the correct number of objects be detected (in this case 1). For SNR 2.5 and 1.5, we found that this was indeed the case for all tested images, both with the active surfaces and the model-free method. At the low SNR of 0.5, however, the model-free method produces on average 10 objects (connected components) [see, e.g., Fig. 2(c)]; in contrast, the active surface method detects

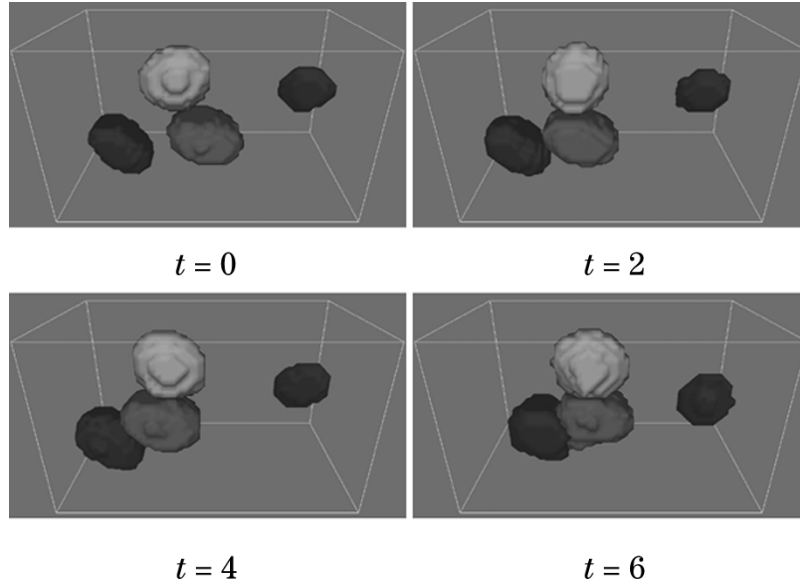


Fig. 7. Tracking touching nuclei. The three nuclei on the left of the image are isolated from each other at  $t = 0$ , then move together and touch ( $t = 4 - 6$ ). Note that the identity of the three touching nuclei is well preserved by the coupled active surfaces, despite minor segmentation errors visible at  $t = 6$ .

exactly one object on all tested images [e.g., Fig. 2(d)], as desired.

Next, we quantified the quality of the segmented surfaces by computing the proportion of misclassified voxels (relative to the true number of object voxels) and their distance from the true object boundary. Results are given in Table I. It can be seen that the active surfaces systematically achieve equal or lower errors than the model-free method. With both methods, errors increase with decreasing SNR, as expected. The proportion of all misclassified voxels are a few percent for SNR 2.5, but become more substantial ( $>10\%$ ) for SNR 0.5. However, most of these errors are concentrated around the object boundary. If we ignore misclassifications at a distance of less than 1 (respectively 2) voxels from the true surface, both methods produce average errors below 1% (respectively 0.1%) for SNR 1.5 and 2.5. The superiority of active surface segmentation over the model-free method is most pronounced at the lowest SNR, where misclassification errors at distances  $<2$  drop to 0.6%, compared to 4% with the model-free alternative. In summary, the overall shape of objects is, thus, well restituted by our active surface method, even at SNR levels for which the object boundaries are hardly visible by eye, and compares quite favorably to the model-free method.

#### D. Tracking Performance on 3-D+Time Data

We now evaluate the ability of our method to track moving cell-like objects undergoing occasional contacts. For this purpose, we generated 30 image sequences of 10  $z$  stacks each, containing two initially separated objects that later on move in contact, before separating again (see Section III-B and Fig. 3). We first checked if the identity of tracked objects was preserved despite the contact event, i.e., if the active surface tracking the object after the contact is the same as before the event. We found that this was the case for all tested image sequences. Note that a single level set method would lose object identity as soon as the objects touch, as we illustrated previously on 2-D images [39].

The same is true for model-free segmentation methods such as the one used in Section III-C above.

Next, we evaluate the quality of segmentation of these contact sequences. Results are presented in Table II. Since two active surfaces are present, one can distinguish two types of classification errors: i) voxels belonging to one of the two objects that are incorrectly assigned to the background, or vice-versa (“background/cells confusion”) and ii) voxels belonging to one object and incorrectly assigned to the other (“cell/cell confusion”).

From the values in Table II, we note that confusions of cells and background are roughly as low here as for segmentation of static 3-D images (Section III-C). Cell/cell confusions before, during and after contact are also very small, indicating that the individual cells are correctly detected before they touch, and again after they separate. It is unsurprising that the largest cell/cell confusions occur when the two objects touch, since they have indistinguishable image properties by construction. These errors are nevertheless small, thanks largely to the volume conservation constraint, allowing both active surfaces to snap back to the correct object when the objects separate again, and resulting in zero confusion errors later in the sequence. An illustration of a test sequence and its processing result is shown in Fig. 3.

Note that the model-free segmentation method used for comparison in Section III-C would merge both objects as soon as they touch. Thus, basic tracking schemes based on the result of these segmentations, such as nearest neighbor matching, would necessarily fail.

#### IV. ILLUSTRATION ON REAL DATA

In this section, we show two examples of real microscopy data from current biological research to illustrate the application of the coupled active surfaces to cellular imaging.

The first example data (Figs. 4 and 5) show cells of the human parasite *Entamoeba histolytica*. Unknown factors cause this amoeba to invade and destroy human tissue, and the study

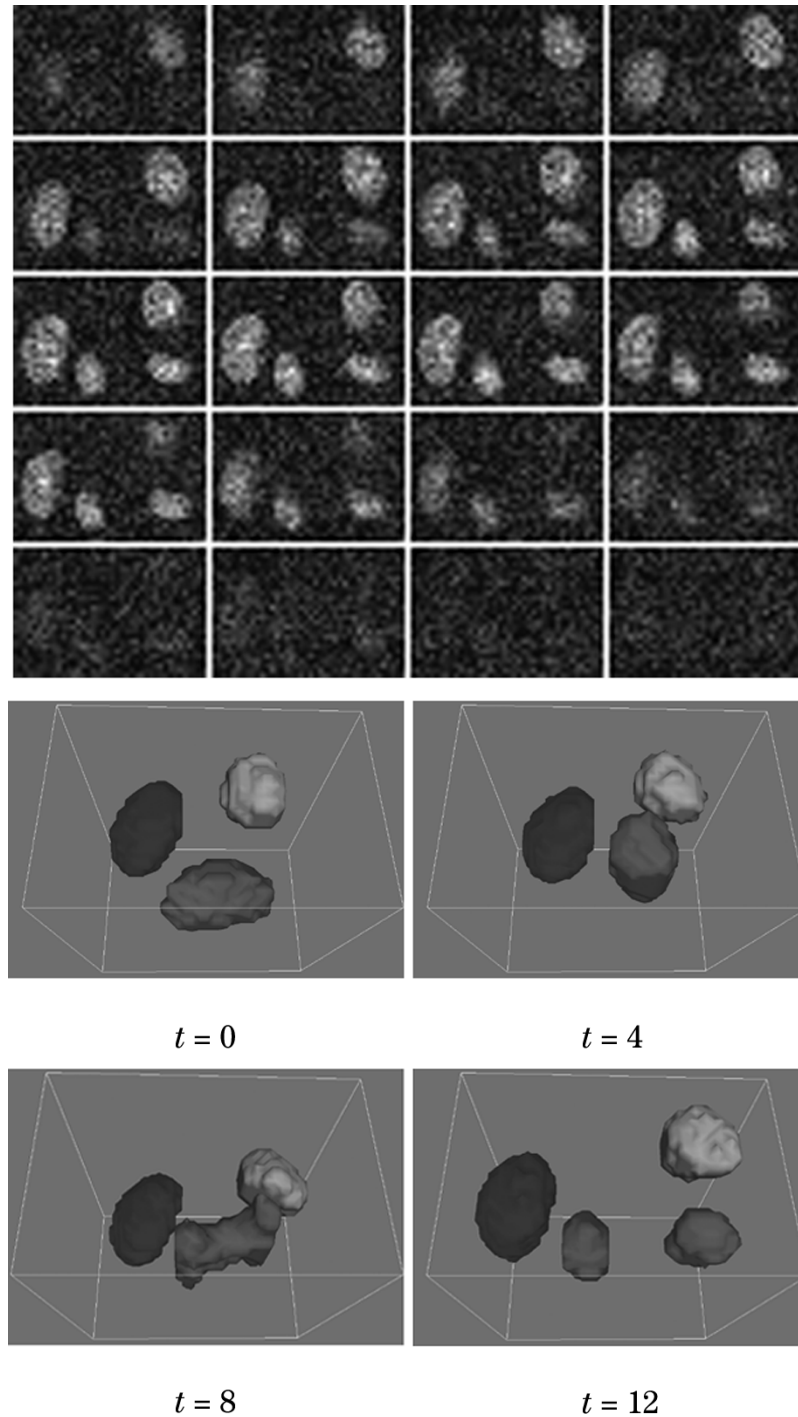


Fig. 8. Tracking dividing nuclei. Top: Montage of 20 of the 40 image slices of the  $z$  stack for  $t = 12$ . Bottom: Segmentation results. The red surface is the segmented nucleus of a cell undergoing mitosis at time  $t = 8$ . The two daughter cells are fully separated at time  $t = 12$ .

of its motility and morphology in a realistic 3-D environment is important for understanding its mechanisms of virulence. Amoebae labeled with a cytoplasmic fluorescent marker (CellTracker Orange CMTMR) were imaged by two-photon microscopy inside 3-D sections of an explanted hamster liver (see details in [4]). Fig. 4 shows an example  $z$  stack together with the segmentation result. Note how the number of cells and their overall shape are correctly restituted despite the relatively low SNR of the raw data. Fig. 5 shows a fragment of a 3-D+time data set where two amoebae undergo a quascontact event: ini-

tially separated, they move in close proximity, and then move away from each other again. The segmentation results illustrate the ability of the coupled active surfaces to maintain the identity of the two cells throughout the image sequence.

The second example (Figs. 6–8) shows confocal spinning disk observations of proliferating MDCK cells, epithelial cells derived from adult dog kidney [51]. Characterizing the random or deterministic 3-D geometry of cell positioning and the timing of cell divisions is important to understand the regulation of tissue and organ growth and repair. Examples of such analyses

using a different, manually assisted segmentation and tracking system, have been described in [52]. The close proximity of cells in a developing tissue makes it very difficult to automatically distinguish and track individual cells using labeling of their membrane or cytoplasm, because the fluorescent signal either belongs to several touching cells or shows no significant gradients across inter-cellular boundaries. To circumvent this problem, we used fluorescently labeled nuclei as readouts of cell positions since nuclei are often spatially isolated or share smaller contact surfaces because of their mostly convex shapes (see Fig. 6). This was done by transfecting the cells with a plasmid that expresses the red fluorescent protein fused to the mouse histone protein H2B (gift by R. Tsien; details to be published elsewhere), which associates with nuclear genomic material. Fig. 6 shows the segmentation of nuclei from a static 3-D image. Fig. 7 shows that initially isolated nuclei can be tracked correctly in spite of close juxtaposition later in the sequence. Fig. 8 shows that cell divisions are naturally handled as a consequence of the level set representation. This potentially permits the construction of cell lineage trees, from which the relationship of individual cells to their ancestors can be analyzed.

## V. CONCLUSION

We have presented a fully automated technique for segmenting and tracking cells in 3-D+time microscopy data. The method uses coupled active surfaces with or without edges together with a volume conservation constraint and several optimizations. Among the chief advantages of this method are the ability to handle touching cells, dividing cells, cells entering the field of view during the sequence, and strong robustness to image noise. We have evaluated the segmentation and tracking performance of the technique using synthetic data and illustrated it on real data from biological imaging.

Significant room for improvement remains to remove several important restrictions. First, since the method still relies on the existence of an image background, it is ill adapted to tight cell clusters such as those occurring in tissue. This could be addressed by staining both nuclei and membranes as in [24] and using an additional active surface to outline the cell boundaries coupled to active surfaces targeting the nuclei. Inclusion of additional image constraints such as motion is also likely to improve outlining of intercellular boundaries. Second, the *a priori* constraints on surface and volume are less suited to outline cell boundaries with high curvature such as filopodia. Third, our method does not yet take into account knowledge of the microscope PSF, which could be used to improve segmentation. Finally, automatic setting of the methods parameters remains an important unresolved issue. We plan to address some of these limitations in subsequent work.

## ACKNOWLEDGMENT

The authors would like to thank the four anonymous referees for suggestions that lead to substantial improvements of the manuscript. They would also like to thank B. Zhang, S. Berlemont, and E. Labrüyère for useful discussions. The marching cube algorithm used for some of the 3-D visualization

was implemented by S. Cousquer. The two photon imaging data (Figs. 4 and 5) were obtained with the help of P. Roux of Plateforme d'Imagerie Dynamique at Institut Pasteur (PFID). The confocal spinning disk data (Figs. 6–8) were acquired with the help of C. Blackmore (Perkin Elmer, U.K.) and L. Luzerno (HiTec-Consulting, Italy) during a workshop organized by the PFID and funded by the European Commission as a part of the European Advanced Microscopy Network (EAMNET).

## REFERENCES

- [1] A. Roumier, J.-C. Olivo-Marin, M. Arpin, F. Michel, P. Mangeat, O. Acuto, A. Dautry-Varsat, and A. Alcove, "The membrane-microfilament linker ezrin is involved in the formation of the immunological synapse and in T cell activation," *Immunity*, vol. 15, pp. 715–728, 2001.
- [2] T. F. Haydar, E. Ang, and P. Rakic, "Mitotic spindle rotation and mode of cell division in the developing telencephalon," *PNAS*, vol. 100, no. 5, pp. 2890–2895, Mar. 2003.
- [3] K. Wolf, I. Mazo, H. Leung, K. Engelke, U. H. von Andrian, E. I. Deryugina, A. Y. Strongin, E. B. Brocker, and P. Friedl, "Compensation mechanism in tumor cell migration: mesenchymal-amoeboid transition after blocking of pericellular proteolysis," *J. Cell Biol.*, vol. 160, no. 2, pp. 267–277, Jan. 2003.
- [4] E. Coudrier, F. Amblard, C. Zimmer, P. Roux, J.-C. Olivo-Marin, M.-C. Rigotherier, and N. Guillén, "Myosin II and the Gal-GalNAc lectin play a crucial role in tissue invasion by Entamoeba histolytica," *Cell. Microbiol.*, vol. 7, no. 1, pp. 19–27, 2005.
- [5] F. Frischknecht, P. Baldacci, B. Martin, C. Zimmer, S. Thiberge, J.-C. Olivo-Marin, S. L. Shorte, and R. Menard, "Imaging movement of malaria parasites during transmission by Anopheles mosquitoes," *Cell. Microbiol.*, vol. 6, no. 7, pp. 687–694, Jul. 2004.
- [6] D. Vlachou, T. Zimmermann, R. Cantera, C. J. Janse, A. P. Waters, and F. C. Kafatos, "Real-time, in vivo analysis of malaria ookinete locomotion and mosquito midgut invasion," *Cell. Microbiol.*, vol. 6, no. 7, pp. 671–685, Jul. 2004.
- [7] E. Sahai and C. J. Marshall, "Differing modes of tumour cell invasion have distinct requirements for rho/rock signalling and extracellular proteolysis," *Nat. Cell Biol.*, vol. 5, no. 8, pp. 711–719, 2003.
- [8] J. Pawley, Ed., *Handbook of Biological Confocal Microscopy*, 2nd ed. New York: Plenum, 1995.
- [9] D. Gerlich and J. Ellenberg, "4D imaging to assay complex dynamics in live specimens," *Nat. Cell Biol.*, pp. S14–S19, Sep. 2003.
- [10] P. Roux, S. Muentner, F. Frischknecht, P. Herbolme, and S. L. Shorte, "Focusing light on infection in four dimensions," *Cell. Microbiol.*, vol. 6, no. 4, pp. 333–343, Apr. 2004.
- [11] G. Brakenhoff and K. Visscher, "Real-time stereo (3D) confocal microscopy," in *Handbook of Biological Confocal Microscopy*, J. Pawley, Ed. New York: Plenum, 1995, pp. 355–362.
- [12] R. B. Dickinson and R. T. Tranquillo, "Optimal estimation of cell movement indices from the statistical analysis of cell tracking data," *AIChE J.*, vol. 39, no. 12, pp. 1995–2010, 1993.
- [13] T. Killich, P. J. Plath, X. Wei, H. Bultmann, L. Rensing, and M. G. Vicker, "The locomotion, shape and pseudopodial dynamics of unstimulated Dictyostelium cells are not random," *J. Cell Sci.*, vol. 106, pp. 1005–1013, Dec. 1993.
- [14] M. Kass, A. Witkin, and D. Terzopoulos, "Snakes: active contour models," *Int. J. Comput. Vis.*, vol. 1, pp. 321–331, 1988.
- [15] A. Blake and M. Isard, *Active Contours*. New York: Springer, 1998.
- [16] T. McInerney and D. Terzopoulos, "Deformable models," in *Handbook of Medical Imaging*, I. Bankman, Ed. New York: Academic, 2000, pp. 127–145.
- [17] S. Osher and N. Paragios, Eds., *Geometric Level Set Methods*. New York: Springer, 2003.
- [18] F. Leymarie and M. D. Levine, "Tracking deformable objects in the plane using an active contour model," *IEEE Trans. Pattern Anal. Mach. Intell.*, vol. 15, no. 6, pp. 617–634, Jun. 1993.
- [19] K. Giuliano, R. DeBiasio, P. Feineigle, and D. Taylor, "Toward the automated dissection of morphological and molecular dynamics of living normal and transformed cells," in *Motion Analysis of Living Cells*, D. R. Soll and D. Wessels, Eds. New York: Wiley, 1998, pp. 53–65.
- [20] N. Ray, S. Acton, and K. Ley, "Tracking leukocytes in vivo with shape and size constrained active contours," *IEEE Trans. Med. Imag.*, vol. 21, no. 10, pp. 1222–1235, Oct. 2002.

- [21] C. Zimmer, E. Labruière, V. Meas-Yedid, N. Guillén, and J.-C. Olivo-Marin, "Segmentation and tracking of migrating cells in videomicroscopy with parametric active contours," *IEEE Trans. Med. Imag.*, vol. 21, no. 10, pp. 1212–1221, Oct. 2002.
- [22] O. Debeir, I. Camby, R. Kiss, P. V. Ham, and C. Decaestecker, "A model-based approach for automated in vitro cell tracking and chemotaxis analyzes," *Cytometry*, vol. 60A, pp. 29–40, 2004.
- [23] C. Zimmer and J.-C. Olivo-Marin, "Coupled parametric active contours," *IEEE Trans. Pattern Anal. Mach. Intell.*, to be published.
- [24] C. Ortiz De Solorzano, R. Malladi, S. A. Lelièvre, and S. J. Lockett, "Segmentation of nuclei and cells using membrane related protein markers," *J. Microsc.*, vol. 201, no. 3, pp. 404–415, Mar. 2001.
- [25] N. Paragios and R. Deriche, "Geodesic active contours and level sets for the detection and tracking of moving objects," *IEEE Trans. Pattern Anal. Mach. Intell.*, vol. 22, no. 3, pp. 266–280, Mar. 2000.
- [26] R. Malladi, J. Sethian, and B. Vemuri, "Shape modeling with front propagation: a level set approach," *IEEE Trans. Pattern Anal. Mach. Intell.*, vol. 17, no. 2, pp. 158–175, Feb. 1995.
- [27] V. Caselles, R. Kimmel, and G. Sapiro, "Geodesic active contours," *Int. J. Comput. Vis.*, vol. 22, no. 1, pp. 61–79, 1997.
- [28] C. Chesnaud, P. Refregier, and V. Boulet, "Statistical region snake-based segmentation adapted to different physical noise models," *IEEE Trans. Pattern Anal. Mach. Intell.*, vol. 21, no. 11, pp. 1145–1157, Nov. 1999.
- [29] C. Samson, L. Blanc-Féraud, G. Aubert, and J. Zerubia, "A level set model for image classification," *Int. J. Comput. Vis.*, vol. 40, no. 3, pp. 187–198, 2000.
- [30] N. Paragios, "Coupled geodesic active regions for image segmentation: a level set approach," in *Proc. Eur. Conf. Comput. Vis.*, 2001, pp. 224–240.
- [31] T. Chan and L. Vese, "Active contours without edges," *IEEE Trans. Image Process.*, vol. 10, no. 2, pp. 266–277, Feb. 2001.
- [32] A. Chakraborty, L. H. Staib, and J. S. Duncan, "Deformable boundary finding in medical images by integrating gradient and region information," *IEEE Trans. Med. Imag.*, vol. 15, no. 6, pp. 859–870, Jun. 1996.
- [33] D. Terzopoulos, "Deformable models: classic, topology-adaptive and generalized formulations," in *Geometric Level Set Methods in Imaging, Vision and Graphics*, S. Osher and N. Paragios, Eds. New York: Springer, 2003, pp. 21–40.
- [34] S. Osher and J. Sethian, "Fronts propagating with curvature-dependent speed: algorithms based on Hamilton-Jacobi formulations," *J. Comput. Phys.*, vol. 79, pp. 12–49, 1988.
- [35] H. Delingette and J. Montagnat, "Shape and topology constraints on parametric active contours," *Comput. Vis. Image Understand.*, vol. 83, pp. 140–171, 2001.
- [36] X. Zeng, L. Staib, R. Schultz, and J. Duncan, "Segmentation and measurement of the cortex from 3-D MR images using coupled-surfaces propagation," *IEEE Trans. Med. Imag.*, vol. 18, no. 10, pp. 927–937, Oct. 1999.
- [37] R. Goldenberg, R. Kimmel, E. Rivlin, and M. Rudzsky, "Cortex segmentation: A fast variational geometric approach," *IEEE Trans. Med. Imag.*, vol. 21, no. 12, pp. 1544–1551, Dec. 2002.
- [38] X. Han, C. Xu, and J. Prince, "A topology preserving level set method for geometric deformable models," *IEEE Trans. Pattern Anal. Mach. Intell.*, vol. 25, no. 6, pp. 755–768, Jun. 2003.
- [39] B. Zhang, C. Zimmer, and J.-C. Olivo-Marin, "Tracking fluorescent cells with coupled geometric active contours," in *Proc. IEEE Int. Symp. Biomed. Imag.*, 2004, pp. 476–479.
- [40] H. Zhao, T. Chan, B. Merriman, and S. Osher, "A variational level set approach to multiphase motion," *J. Comput. Phys.*, vol. 127, no. 1, pp. 179–195, 1996.
- [41] L. Vese and T. Chan, "A multiphase level set framework for image segmentation using the Mumford and Shah model," *Int. J. Comput. Vis.*, vol. 50, no. 3, pp. 271–293, 2002.
- [42] A. Yezzi, A. Tsai, and A. Willsky, "A fully global approach to image segmentation via coupled curve evolution equations," *J. Vis. Commun. Image Represen.*, vol. 13, no. 1/2, pp. 195–216, Mar./Jun. 2002.
- [43] D. Mukherjee, N. Ray, and S. Acton, "Level set analysis for leukocyte detection and tracking," *IEEE Trans. Image Process.*, vol. 13, no. 4, pp. 562–572, Apr. 2004.
- [44] K. Strange, "Cellular volume homeostasis," *Adv. Physiol. Edu.*, vol. 28, pp. 155–159, 2004.
- [45] D. Chopp, "Computing minimal surfaces via level set curvature flow," *J. Comput. Phys.*, vol. 106, pp. 77–91, 1993.
- [46] D. Adalsteinsson and J. Sethian, "A fast level set method for propagating interfaces," *J. Comput. Phys.*, vol. 118, no. 2, pp. 269–277, 1995.
- [47] J. Sethian, *Level Set Methods and Fast Marching Methods*. New York: Cambridge Univ. Press, 1999.
- [48] B. Song, "Topics in variational PDE image segmentation, inpainting and denoising," Ph.D. dissertation, Dept. Math., Univ. California, Los Angeles, Jun. 2003.
- [49] P. Perona and J. Malik, "Scale space and edge detection using anisotropic diffusion," *IEEE Trans. Pattern Anal. Mach. Intell.*, vol. 12, no. 5, pp. 629–639, May 1990.
- [50] N. Otsu, "A threshold selection method from gray level histograms," *IEEE Trans. Syst., Man, Cybern.*, vol. 9, no. 1, pp. 62–66, Jan. 1979.
- [51] J. Leighton, Z. Brada, L. Estes, and G. Justh, "Secretory activity and oncogenicity of a cell line (MDCK) derived from canine kidney," *Science*, vol. 163, no. 866, pp. 472–473, 1969.
- [52] P. J. Heid, E. Voss, and D. R. Soll, "3D-DIASemb: a computer-assisted system for reconstructing and motion analyzing in 4D every cell and nucleus in a developing embryo," *Develop. Biol.*, vol. 245, no. 2, pp. 329–347, May 2002.



**Alexandre Dufour** received the B.S. degree in computer science in 2002 and the M.S. degree in artificial intelligence and pattern recognition in 2004 from the Pierre et Marie Curie University, Paris, France. He is currently pursuing the Ph.D. degree at the Institut Pasteur Korea, Seoul.

His main research interests are 3-D/4-D segmentation and tracking techniques and their applications to biological image processing.

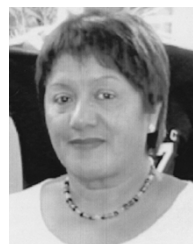


**Vasily Shinin** received the M.D. degree from Russian State Medical University and the Ph.D. degree in cell biology from Koltsov Institute of Developmental Biology, Moscow, Russia.

He is currently a Postdoctoral Researcher in the Stem Cells and Development Laboratory, with Dr. S. Tajbakhsh, at the Pasteur Institute, Paris, France.

**Shahragim Tajbakhsh** received the Ph.D. degree in biology from Carleton University and the National Research Council of Canada, Ottawa, ON, for work on the molecular and cellular biology of Tipula iridescent virus.

In January 1990, he joined the Pasteur Institute, Paris, France, where he worked on skeletal muscle development in mice, and where he obtained a research position in 1995. Since September 2001, he has been directing the Laboratory of Stem Cells and Development, Pasteur Institute, where he is pursuing his interests in investigating how skeletal muscle identity is established from stem cells and how stem and progenitors are regulated and how they self renew. The principal approaches involve using combinations of mutant mice, cell, and molecular biology techniques, coupled with live imaging of cell-fate events.



**Nancy Guillén-Aghion** received the M.S. degree from the Central University of Caracas, Caracas, Venezuela, and the Docteur d'Etat degree (Ph.D.) degree from the Paris Sud University, Orsay, France.

She is a Research Director at the National Center of Scientific Research (CNRS), and she heads the Cellular Biology of Parasitism Unit at the Institut Pasteur, Paris, France. Her goal is to understand the molecular and cellular mechanisms that allow human tissue invasion by *Entamoeba histolytica*, the agent of amoebiasis. She is particularly interested in

understanding how parasites displace themselves by analysing chemoattractant molecules, cytoskeleton dynamics, and parasite morphological changes during infection of human tissues.



**Jean-Christophe Olivo-Marin** (SM'93) received the Ph.D. degree and the "Habilitation à Diriger des Recherches" from the Institut d'Optique Théorique et Appliquée, University of Paris-Orsay, Orsay, France, in 1989 and 1998, respectively.

He is the Head of the Quantitative Image Analysis Group, Institut Pasteur, Paris, France. From 2004 to 2005, he had a joint appointment as Chief Technology Officer, Institut Pasteur Korea, Seoul. From 1990 to 1998, he was a Staff Scientist at the European Molecular Biology Laboratory, Heidelberg,

Germany. His research interests are in image processing and computer vision applied to biological image analysis, with special emphasis on multiresolution processing, image segmentation, and video microscopy sequence analysis.

He is a member of SPIE and the Pattern Recognition Society.



**Christophe Zimmer** received the Ph.D. degree in astrophysics and space techniques from the Université Paris 7, Paris, France, for a study on planetary magnetosphere theory done at the Observatoire Midi-Pyrénées, Toulouse, France.

From 1998 to 2000, he worked on analyzing and modeling Jupiter's magnetic field as Assistant Research Geophysicist in M. G. Kivelson's group at the University of California, Los Angeles. At the end of 2000, he joined the Quantitative Image Analysis Group at the Institut Pasteur, Paris, where he has

been a Permanent Researcher since 2003. His interests are in developing methods to extract quantitative information from dynamic imaging data and in analyzing them to help understand biological processes.